doi:10.1038/nature14463

Quantum coherent optical phase modulation in an ultrafast transmission electron microscope

Armin Feist[1], Katharina E. Echternkamp[1], Jakob Schauss[1], Sergey V. Yalunin[1], Sascha Schäfer[1] & Claus Ropers[1]

Coherent manipulation of quantum systems with light is expected to be a cornerstone of future information and communication technology, including quantum computation and cryptography[1]. The transfer of an optical phase onto a quantum wavefunction is a defining aspect of coherent interactions and forms the basis of quantum state preparation, synchronization and metrology. Light-phase-modulated electron states near atoms and molecules are essential for the techniques of attosecond science, including the generation of extreme-ultraviolet pulses and orbital tomography[2,3]. In contrast, the quantum-coherent phase-modulation of energetic free-electron beams has not been demonstrated, although it promises direct access to ultrafast imaging and spectroscopy with tailored electron pulses on the attosecond scale. Here we demonstrate the coherent quantum state manipulation of free-electron populations in an electron microscope beam. We employ the interaction of ultrashort electron pulses with optical near-fields[4–9] to induce Rabi oscillations in the populations of electron momentum states, observed as a function of the optical driving field. Excellent agreement with the scaling of an equal-Rabi multilevel quantum ladder is obtained[10], representing the observation of a light-driven 'quantum walk'[5] coherently reshaping electron density in momentum space[11]. We note that, after the interaction, the optically generated superposition of momentum states evolves into a train of attosecond electron pulses. Our results reveal the potential of quantum control for the precision structuring of electron densities, with possible applications ranging from ultrafast electron spectroscopy and microscopy to accelerator science and free-electron lasers.

The interaction of propagating light with confined electrons in atoms, molecules and solids is omnipresent, but the opposite case—the coupling of free electrons to localized optical fields—is not a naturally occurring phenomenon. Nonetheless, in both cases, the principle of confinement allows for optical transitions in otherwise mismatched electron and photon dispersion relations[12]. Controlling free-electron propagation with low-frequency electromagnetic fields in resonator geometries is an integral aspect of accelerator science[13]. At optical frequencies, however, particular challenges arise from the requirements of very controlled electron beams and tailored nanostructure near-fields. Increasing efforts are currently devoted to optically drive electron trajectories on the nanoscale—for example, for applications in attosecond science and lightwave electronics[14–19].

Some of the elementary phenomena involved in coupling free electrons to light were described more than half a century ago: in the Kapitza–Dirac effect[20,21], electrons are elastically scattered off a standing light wave, whereas the Smith–Purcell effect and its variants[8,9,22,23] treat the inelastic interaction of free electrons with confined modes close to a grating. Recently, ultrafast electron microscopy schemes showed that the kinetic energy distribution of short electron pulses develops a series of photon sidebands after passage through an intense optical near-field[4–6]. This approach, termed photon-induced near-field electron microscopy (PINEM)[4], has been employed in the temporal characterization of ultrashort electron pulses (see Methods) and as a contrast mechanism in electron microscopy[24,25]. Beyond such advanced applications, the underlying interaction should allow for the preparation of coherent electronic superposition states and a phase-controlled harnessing of quantum coherence for the temporal shaping of electron bunches.

Here we report the coherent phase-modulation of free-electron states in a nano-optical field. We experimentally induce multilevel Rabi oscillations in the form of a quantum walk in momentum space, obtaining excellent agreement with theoretical predictions by García de Abajo *et al.*[5] and Park *et al.*[6] of this interaction. Moreover, we demonstrate theoretically that dispersive propagation transforms the optically modulated electron wavepacket into a train of attosecond peaks. In the experimental scenario displayed in Fig. 1, femtosecond electron pulses are generated by nonlinear photoemission from a nanoscale cathode[26–28]. After collimation and acceleration to an energy of 120 keV, the magnetic lens system of a transmission electron microscope focuses the electron pulses to a spot diameter of 15 nm in close vicinity to an optically excited conical gold tip. The localization of the nanostructure's near-field mediates the optical interaction with the free electrons. This leads to the creation of multiple spectral sidebands, each corresponding to the absorption/emission of an integer number of photons (spectrum in Fig. 1e)[4–6]. Detailed information about the interaction process is encoded in the number of populated sidebands and their individual amplitudes. For example, the maximum electron energy gain in the optical near field is a quantitative measure of the local transition amplitude, which can be imaged by raster scanning the electron focus (Fig. 1b).

Microscopically, the electron–light interaction studied here constitutes an optical phase-modulation of the electron wavefunction[6]. Expressed as a quantum mechanical multilevel system, electron energy levels spaced by the photon energy $\hbar\omega$ are coupled in the optical near-field (level diagram, Fig. 1d). Previous experiments studying this interaction found a partial reduction of the initial electronic state population and a spectral broadening with distributions gradually decaying towards large photon orders[4,6,7,24,25]. Such observations evidence transitions dominated by sequential multilevel excitation (processes of type I in Fig. 1d). However, it is assumed that the coupling process is coherent in nature[5,6], which implies that quantum features arising from multipath interference (type II) should also be observable.

In order to identify such phenomena, we require an interaction of uniform strength with the entire electron ensemble in the pulse[5]. This scenario is achieved by using a spatially narrow probing beam and, in contrast to earlier works, an optical near-field excitation which has a uniform amplitude during the transit of the electron pulse envelope (see Methods).

Under these conditions, we find experimentally that the population of photon sidebands exhibits a pronounced oscillatory behaviour corresponding to multilevel Rabi oscillations, as demonstrated in Fig. 2 for electron spectra at a fixed position near the tip shaft. A colour-coded map (Fig. 2a) displays the evolution of the interaction-induced kinetic energy distribution with growing incident field strength. With increasing driving field, we observe a linear spreading in the range of

---

[1] 4th Physical Institute, Solids and Nanostructures, University of Göttingen, Göttingen 37077, Germany.

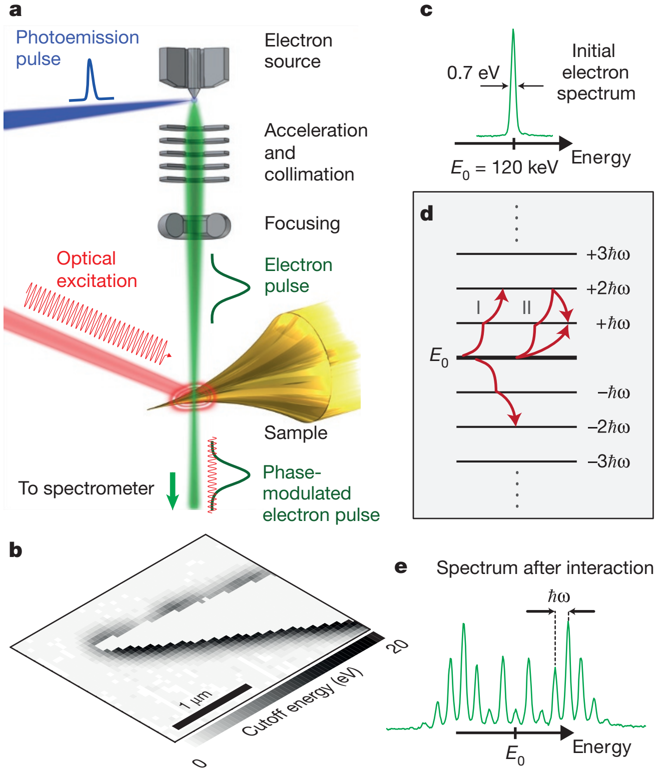

Figure 1 | Schematic and principles of coherent inelastic electron scattering by optical near-fields. **a**, Experimental scheme. Ultrashort electron pulses generated by nanotip photoemission are accelerated and focused to a beam that interacts with the optical near-field of a nanostructure, phase-modulating the electron pulse and exchanging energy in integer multiples of the photon energy. **b**, Raster-scanned image of the energy cutoff in the inelastic electron scattering spectra, representing the local transition amplitude (see text). **c**, Incident kinetic energy spectrum (full-width at half-maximum, 0.7 eV) centred at $E_0 = 120$ keV. **d**, Energy level diagram of ladder states with spacing $\hbar\omega$ coupled to the initial state at E_0. Arrows indicate sequential multistate population transfer (type I) and interfering quantum paths (type II) leading to multilevel Rabi oscillations. **e**, Example of kinetic energy spectrum after the near-field interaction, exhibiting a spectral comb with multiple sidebands separated by the photon energy and modulated in occupation.

populated sidebands, together with strong oscillations in the central part of the spectra. Specifically, the experimental spectra exhibit a nearly complete extinction of the initial state occupation and its pronounced recurrence at incident fields of 0.023 V nm^{-1} (red line) and 0.040 V nm^{-1} (green line), respectively (Fig. 2c). Quantitative analysis of the field-dependent spectral evolution (Fig. 2b) shows the oscillations of the initial state population ('zero loss peak') and those of different electronic sidebands. These modulations directly evidence multilevel Rabi oscillations and thereby a quantum coherent manipulation of the respective level amplitudes, which, as a function of field strength, traces out the evolution of an elementary quantum walk[11].

Recently, near-field-induced free-electron transitions, as observed here, were theoretically treated by solving the time-dependent Schrödinger equation[5,6] (compare our results to figure 2 in ref. 5, which depicts population oscillations simulated as a function of intensity). Yielding equivalent theoretical results, we present a compact description using raising and lowering operators acting on the electronic state $|E_0\rangle$ of the system at an initial energy E_0. As demonstrated in the Methods section, the action of the near-field can be described by a scattering matrix $S = \exp[g^*a - ga^\dagger]$ with a dimensionless near-field coupling constant g proportional to the field strength and the transition matrix element. One may notice that S takes the

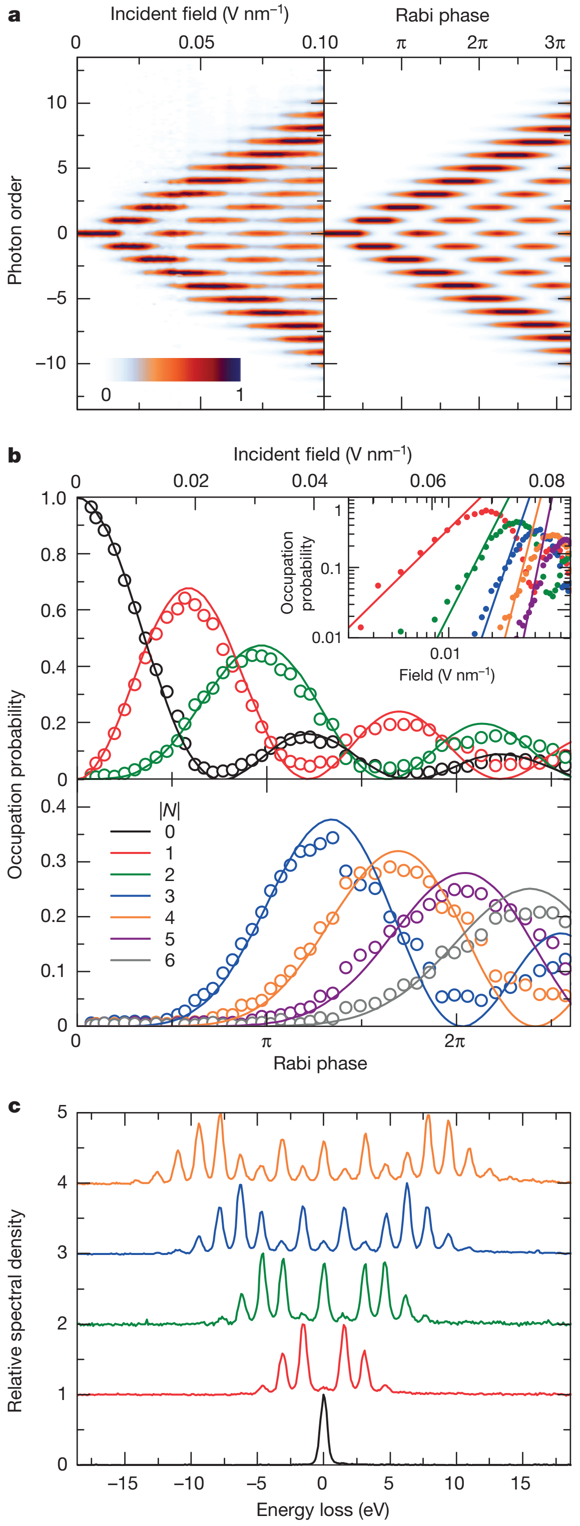

Figure 2 | Quantum coherent manipulation of electron energy distributions. **a**, Experimental electron energy distributions as a function of the incident optical field strength (left) and theoretical prediction in terms of Nth-order Bessel functions (right). **b**, Occupation probabilities (open circles) of the Nth-order spectral sidebands shown in **a**, adding contributions from $\pm|N|$. Solid lines, Nth-order Bessel functions. Inset, double-logarithmic plot of the sideband populations near onset. Solid lines with slope $2N$ are shown for comparison. **c**, Electron energy spectra at incident optical fields of 0, 0.023, 0.040, 0.053 and 0.068 V nm^{-1} (bottom to top). Spectra shown in **a** and **c** are normalized to their respective maxima.

form of a displacement operator generating coherent states in the harmonic oscillator model. In a variation of this scenario, we use $a^\dagger$ and a as commuting raising and lowering operators, connecting free-electron states separated by the photon energy, that is, $a^\dagger|E_0\rangle = |E_0 + \hbar\omega\rangle$ and $a|E_0\rangle = |E_0 - \hbar\omega\rangle$. The scattering matrix represents the Hamiltonian evolution of the system as a unitary operation on the initial electron wavefunction $|E_0\rangle$, which leaves the electron in a superposition of ladder states $|E_0 \pm N\hbar\omega\rangle$, with N a natural number.

In the limit of small optical driving fields, the scattering matrix is dominated by sequential multiphoton terms, for example, $\frac{1}{N!}\left(ga^\dagger\right)^N$, corresponding to type I transitions (Fig. 1d). The occurrence of interfering quantum paths at increased optical field strength (type II paths) becomes apparent by considering higher order terms in the Taylor expansion of S, such as $a^\dagger$ and $a^\dagger a^\dagger a$, which both facilitate the transition between the states $|E_0\rangle$ and $|E_0 + \hbar\omega\rangle$, but each with a different phase factor in the final state.

Interestingly, because of the practically constant coupling matrix elements between adjacent levels (the 'equal Rabi' case[10]), the occupation probability of the Nth photon sideband can be described by a very simple analytical expression in the form of the Nth-order Bessel function of the first kind[5,6], that is, $|\langle E_0 \pm N\hbar\omega|S|E_0\rangle|^2 = |J_N(2|g|)|^2$. In a spatial representation, these transitions arise from a sinusoidal phase modulation of the wavefunction traversing the optical near-field. Accordingly, such sideband populations are also commonly encountered in other physical systems using phase modulation, for example, in acousto-optics[29].

Comparing the experimental field-dependent electron populations with the analytical result (Fig. 2b), an excellent agreement is found both in the location and amplitudes of the respective occupation minima/maxima. The entire data set is described with a single Rabi phase $2|g| = F_{\mathrm{inc}} \times 98\,\mathrm{V}^{-1}$ nm linearly increasing with the incident optical field strength F_{inc}, yielding a quantitative measure of the transition matrix element. As detailed in the Methods section, incomplete modulation of the Rabi oscillations at higher fields is caused by the finite spatial and temporal electron pulse widths within the optical near-field. Besides the predicted population oscillations, the characteristic low-field multiphoton limit of the electron–light interaction is also experimentally regained (slopes of $2N$ in the field in a double-logarithmic plot, see inset of Fig. 2b). Larger incident fields prominently transfer the electron distribution to the outer spectral lobes, creating a well-defined cutoff around $|E - E_0| = 2|g|\hbar\omega$, equal to the maximum classical energy transfer. Thus, as in other instances of electrons driven by intense optical near-fields[15,16,19], the interaction energy is governed directly by the field amplitude instead of the ponderomotive energy.

This periodic phase (and correspondingly momentum) modulation of the electron wavefunction has important consequences for its subsequent evolution in free propagation. Generally, momentum modulation of classical states in particle accelerators is used for bunch compression[13], and an optical variant of this principle was recently proposed using ponderomotive forces acting on classical point particles[30]. However, the present conditions with electronic coherence times exceeding the optical period necessitate a quantum mechanical description of bunch reshaping. Figure 3a displays a few cycles of the simulated electron density in a periodically phase-modulated wavepacket as a function of the propagation distance and the arrival time at this distance relative to the centre of the pulse. Specifically, the phased superposition of momentum states reshapes into a high-contrast train of attosecond pulses at a well-defined distance downstream from the interaction region. For typical coupling constants achieved in the experiments, we obtain a temporal focusing into a train of pulses only about 80 as long, at a distance of 1.8 mm behind the sample. Further dispersion spreads the distribution corresponding to its momentum content, with the possibility of revivals. Note that a spatial optical equivalent of this generation of attosecond spikes is given by Fresnel diffraction at a sinusoidal phase grating into a near-field fringe pattern[31], and also that an early theoretical scheme for subfemtosecond optical pulse generation relied on frequency modulation and subsequent reshaping[32].

The physical origin of this electron pulse compression can be illustrated using a phase space representation of the quantum state in the form of a Wigner function. This function is a quantum mechanical analogue of a phase space density, which, however, can also take negative values for non-classical states[33]. Figure 3b displays the Wigner function of one period of a propagated state at the temporal focus and for a typical momentum distribution (projection in Fig. 3c). In this plane, free propagation of the initially sinusoidal momentum modulation has sheared the phase space distribution to a situation where a highly localized projection onto the position axis, that is, arrival time, is formed (Fig. 3d). In fact, the generation of this attosecond electron pulse train is very robust with respect to variations of the specific temporal and energetic structure of the initial electron pulse (see Methods). The practically usable focal distances (a few millimetres) render this scheme directly applicable in electron microscopy or spectroscopy studies with attosecond precision, a domain at present

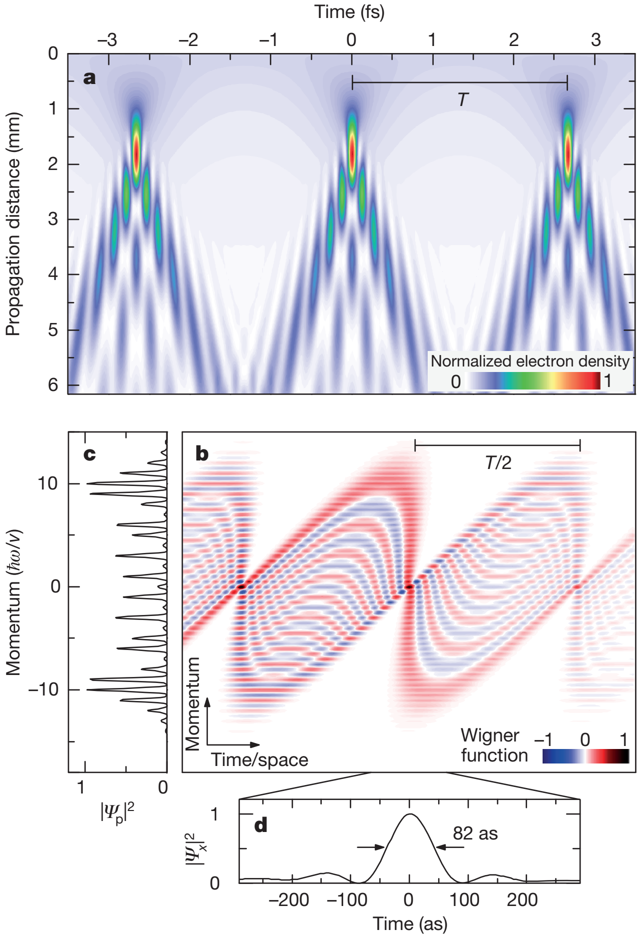

Figure 3 | Formation of an attosecond electron pulse train. a, Development of a periodically modulated electron pulse structure (normalized electron density is colour coded) as a function of the propagation distance after the near-field interaction (numerical simulation for $|g| = 5.7$). Free propagation causes a temporal focusing into a train of attosecond spikes (red) with a period of $T = 2.55$ fs (optical period). **b**, Phase space (Wigner) representation of one period of the light-modulated electron quantum state at the temporal focus position (propagation distance of 1.8 mm in **a**). Note that time and space variables for the swift electron pulse can be used equivalently via $x = vt$ (v is mean electron velocity). **c**, Momentum projection of Wigner function exhibiting spectral modulations as observed in the experiments, displayed in units of transferred momentum quanta (average momentum subtracted). **d**, Central part of spatial projection, expressed in terms of electron arrival time in laboratory frame. A peak with a duration of only 82 as (FWHM) is produced.

only accessible by attosecond light pulses[2]. Specifically, the temporal electron comb will enable the phase-resolved investigation of coherent sample excitations, thus tracing structural or electronic changes carrying optical phase information.

In conclusion, we have demonstrated the quantum coherent manipulation of free-electron wavefunctions by their interaction with nano-confined light fields, observing near-perfect correspondence to the behaviour of a multilevel model Hamiltonian. Thinking beyond a single-variable state control, near-field interactions are expected to cause entanglement of longitudinal and transverse momentum components, and moreover, Coulomb interactions in a beam crossover will result in correlations between multiple electrons. Both features may be crucial for employing free electrons in quantum information technology[1]. Perhaps surprisingly, the generation of an attosecond electron train is a direct and natural consequence of this optical phase-modulation. We anticipate various applications of this concept in imaging and spectroscopy—for example, in the phase-resolved detection of coherent, resonantly driven polarizations in solid state materials—thus opening up the study of attosecond phenomena in electron microscopy.

Online Content Methods, along with any additional Extended Data display items and Source Data, are available in the online version of the paper; references unique to these sections appear only in the online paper.

Received 17 November 2014; accepted 24 March 2015.

1. Bouwmeester, D., Ekert, A. & Zeilinger, A. *The Physics of Quantum Information* (Springer, 2000).
2. Krausz, F. & Ivanov, M. Attosecond physics. *Rev. Mod. Phys.* **81,** 163–234 (2009).
3. Itatani, J. *et al.* Tomographic imaging of molecular orbitals. *Nature* **432,** 867–871 (2004).
4. Barwick, B., Flannigan, D. J. & Zewail, A. H. Photon-induced near-field electron microscopy. *Nature* **462,** 902–906 (2009).
5. García de Abajo, F. J., Asenjo-Garcia, A. & Kociak, M. Multiphoton absorption and emission by interaction of swift electrons with evanescent light fields. *Nano Lett.* **10,** 1859–1863 (2010).
6. Park, S. T., Lin, M. & Zewail, A. H. Photon-induced near-field electron microscopy (PINEM): theoretical and experimental. *New J. Phys.* **12,** 123028 (2010).
7. Kirchner, F. O., Gliserin, A., Krausz, F. & Baum, P. Laser streaking of free electrons at 25 keV. *Nature Photon.* **8,** 52–57 (2013).
8. Peralta, E. A. *et al.* Demonstration of electron acceleration in a laser-driven dielectric microstructure. *Nature* **503,** 91–94 (2013).
9. Breuer, J. & Hommelhoff, P. Laser-based acceleration of nonrelativistic electrons at a dielectric structure. *Phys. Rev. Lett.* **111,** 134803 (2013).
10. Shore, B. W. & Eberly, J. H. Analytic approximations in multi-level excitation theory. *Opt. Commun.* **24,** 83–88 (1978).
11. Bouwmeester, D., Marzoli, I., Karman, G., Schleich, W. & Woerdman, J. Optical Galton board. *Phys. Rev. A* **61,** 013410 (1999).
12. García de Abajo, F. J. Optical excitations in electron microscopy. *Rev. Mod. Phys.* **82,** 209–275 (2010).
13. Hemsing, E., Stupakov, G., Xiang, D. & Zholents, A. Beam by design: laser manipulation of electrons in modern accelerators. *Rev. Mod. Phys.* **86,** 897–941 (2014).
14. Krüger, M., Schenk, M. & Hommelhoff, P. Attosecond control of electrons emitted from a nanoscale metal tip. *Nature* **475,** 78–81 (2011).
15. Herink, G., Solli, D. R., Gulde, M. & Ropers, C. Field-driven photoemission from nanostructures quenches the quiver motion. *Nature* **483,** 190–193 (2012).
16. Wimmer, L. *et al.* Terahertz control of nanotip photoemission. *Nature Phys.* **10,** 432–436 (2014).
17. Schiffrin, A. *et al.* Optical-field-induced current in dielectrics. *Nature* **493,** 70–74 (2012).
18. Piglosiewicz, B. *et al.* Carrier-envelope phase effects on the strong-field photoemission of electrons from metallic nanostructures. *Nature Photon.* **8,** 37–42 (2013).
19. Stockman, M. I., Kling, M. F., Kleineberg, U. & Krausz, F. Attosecond nanoplasmonic-field microscope. *Nature Photon.* **1,** 539–544 (2007).
20. Kapitza, P. L. & Dirac, P. M. The reflection of electrons from standing light waves. *Math. Proc. Camb. Phil. Soc.* **29,** 297–300 (1933).
21. Freimund, D. L., Aflatooni, K. & Batelaan, H. Observation of the Kapitza-Dirac effect. *Nature* **413,** 142–143 (2001).
22. Smith, S. & Purcell, E. Visible light from localized surface charges moving across a grating. *Phys. Rev.* **92,** 1069 (1953).
23. Mizuno, K., Pae, J., Nozokido, T. & Furuya, K. Experimental evidence of the inverse Smith-Purcell effect. *Nature* **328,** 45–47 (1987).
24. Flannigan, D. J., Barwick, B. & Zewail, A. H. Biological imaging with 4D ultrafast electron microscopy. *Proc. Natl Acad. Sci. USA* **107,** 9933–9937 (2010).
25. Yurtsever, A., van der Veen, R. M. & Zewail, A. H. Subparticle ultrafast spectrum imaging in 4D electron microscopy. *Science* **335,** 59–64 (2012).
26. Ropers, C., Solli, D. R., Schulz, C. P., Lienau, C. & Elsaesser, T. Localized multiphoton emission of femtosecond electron pulses from metal nanotips. *Phys. Rev. Lett.* **98,** 043907 (2007).
27. Hommelhoff, P., Kealhofer, C. & Kasevich, M. A. Ultrafast electron pulses from a tungsten tip triggered by low-power femtosecond laser pulses. *Phys. Rev. Lett.* **97,** 247402 (2006).
28. Gulde, M. *et al.* Ultrafast low-energy electron diffraction in transmission resolves polymer/graphene superstructure dynamics. *Science* **345,** 200–204 (2014).
29. Moharam, M. G. & Young, L. Criterion for Bragg and Raman-Nath diffraction regimes. *Appl. Opt.* **17,** 1757–1759 (1978).
30. Baum, P. & Zewail, A. H. Attosecond electron pulses for 4D diffraction and microscopy. *Proc. Natl Acad. Sci. USA* **104,** 18409–18414 (2007).
31. Case, W. B., Tomandl, M., Deachapunya, S. & Arndt, M. Realization of optical carpets in the Talbot and Talbot-Lau configurations. *Opt. Express* **17,** 20966–20974 (2009).
32. Harris, S. E. & Sokolov, A. V. Subfemtosecond pulse generation by molecular modulation. *Phys. Rev. Lett.* **81,** 2894–2897 (1998).
33. Mandel, L. & Wolf, E. *Optical Coherence and Quantum Optics* (Cambridge Univ. Press, 1995).

Acknowledgements We thank M. Sivis and B. Schröder for help with sample preparation. We also thank our colleagues within the Göttingen UTEM initiative (C. Jooß, M. Münzenberg, K. Samwer, M. Seibt, C.A. Volkert). This work was supported by the Deutsche Forschungsgemeinschaft (DFG-SFB 1073/project A05), the VolkswagenStiftung, and the Lower Saxony Ministry of Science and Culture. We thank JEOL Ltd and JEOL Germany for their continuing support during the development of the Göttingen Ultrafast Transmission Electron Microscope.

Author Contributions The experiments were carried out by A.F., with contributions from J.S. and S.S.; S.S. and C.R. conceived and directed the study; S.V.Y. developed the analytical description and K.E.E. carried out the numerical simulations, each with contributions from A.F., S.S. and C.R.; the manuscript was written by A.F., K.E.E., S.S. and C.R., after discussions with and input from all authors.

Author Information Reprints and permissions information is available at www.nature.com/reprints. The authors declare no competing financial interests. Readers are welcome to comment on the online version of the paper. Correspondence and requests for materials should be addressed to S.S. (schaefer@ph4.physik.uni-goettingen.de) or C.R. (cropers@gwdg.de).

METHODS

Ultrafast TEM and experimental setup. We have recently constructed an ultrafast TEM (UTEM) to enable a variety of laser-pump/electron-probe imaging schemes with high spatial resolution. The microscope is based on a commercial Schottky field emission TEM (JEOL JEM-2100F), which we modified to allow for both optical sample excitation and laser-driven electron pulse generation in the gun, as shown in Extended Data Fig. 1. In contrast to previous implementations of time-resolved TEM, our instrument features a nanotip photocathode as the source of ultrashort electron pulses. Compared to planar emitters, such needle cathodes provide reduced electron beam emittance, which is particularly useful for nanoscale probing and spectroscopy. In the present experiments, we employ electron pulses with a repetition rate of 250 kHz, which are induced via two-photon photoemission by irradiating the apex of a tungsten field emission cathode (apex radius of curvature of about 120 nm) with ultrashort laser pulses (400 nm central wavelength, 50 fs pulse duration, 4.1 nJ pulse energy, 25 GW cm^{-2} incident peak intensity). The emitter tip is operated at room temperature and with an electrostatic extraction field of 0.1 V nm^{-1}.

At an electron energy of 120 keV, the beam is focused to a spot diameter of about 15 nm, with a typical electron pulse duration of 700–900 fs (full-width at half-maximum, FWHM) at the position of the sample (characterized by electron–laser cross-correlation, see below). This pulse duration is at present governed by velocity dispersion of electrons with different initial kinetic energies after photoemission, which, however, is not a limitation for the measurements described here. While pulses may contain many electrons, all experiments reported here were acquired with less than one electron per pulse at the sample position (single-electron mode), thus avoiding potential space charge influences.

The laser pulse exciting the optical near-field (central wavelength of 800 nm, pulse energy of up to 60 nJ) is stretched by dispersion in glass to a pulse duration of 3.4 ps and focused to a spot size of ~50 μm, yielding peak intensities of 1.33 GW cm^{-2} at the largest applied fluence. The excitation with a laser pulse of a duration much longer than that of the electron pulse allows for the observation of coherent population oscillations (see section 'Numerical calculations' below).

After interaction with the optical near-field, the electron pulse is imaged (magnification of 25,000) into an electron energy-loss spectrometer (EELS) to analyse its kinetic energy distribution (spectrometer entrance aperture of 3 mm, energy dispersion of 0.05 eV per detector channel).

Modulated electron spectra are observed at any electron probe position within the optical near-field. However, the quality of the spectral modulation and full extinction of individual orders crucially depends on the transverse homogeneity of the near-field on the scale of the electron beam diameter (see section 'Numerical calculations' below). For a nanoscopic tip, the optical near-fields are only slowly varying along its shaft. Therefore, we chose a position of the electron focus several micrometres away from the tip apex (see Extended Data Fig. 2).

Temporal characterization of electron pulses. In UTEM, the duration of the electron pulses is governed mainly by Coulomb repulsion and dispersive broadening within the electron gun and subsequent electron optics. The resulting electron pulse structure in the sample plane can be quantitatively characterized employing inelastic near-field electron scattering[34,35,42], as discussed in the main text. However, to this end, and in contrast to the experimental conditions described in the previous section, laser pulses of a duration (here 50 fs) much shorter than the electron pulse duration should be used in an electron/near-field cross-correlation[35].

Extended Data Fig. 3a displays electron energy spectra as a function of the temporal delay between the optical excitation and the electron pulse arrival, subtracting the electron spectrum in the absence of near-field excitation. Therefore, the central blue feature corresponds to the reduction of the zero-loss peak due to scattering of electrons into multiple photon sidebands (red stripes). The width of these features (Extended Data Fig. 3b) and their tilt in the energy–time diagram (inset) provide measures of the electron pulse duration and chirp, respectively. Here, we obtain a cross-correlation with a FWHM of 800 fs (standard deviation of 340 fs) and a chirp of ~760 fs eV^{-1} for an initial energy spread of 1.3 eV. In the experiments presented in the main text, electron pulses with a narrower energy spread of 0.7 eV were achieved. For the much shorter near-field excitation employed here, the scattering signal is linear in the momentary density of electrons within the pulse. Therefore, we can extract an energy–time representation of the electron pulse by superimposing all tilted sidebands (Extended Data Fig. 3c). Finally, we emphasize that temporally stretching the near-field excitation to more than 3 ps in the experiments ensures that it lasts much longer than the electron pulse duration and, therefore, provides for a nearly homogeneous scattering amplitude throughout the electron pulse.

Data analysis and drift correction. In order to obtain high quality electron spectra at a fixed sample location for varying driving field strengths, it has to be ensured that the laser-induced sample displacement, for example, by thermal expansion, is compensated for. This was achieved by first characterizing the fluence-dependent sample shift in imaging mode (observed up to 150 nm) and by automated electron beam repositioning between experimental runs. In addition, slow residual drifts (up to 20 nm, see Extended Data Fig. 2a) were corrected for by continuous line scans perpendicular to the gold surface and using the strength of the bulk plasmon band to identify the beam–surface distance. In the recorded spectra, energy losses due to bulk plasmon excitation generate a weak and spectrally broad band at energies above 15 eV (ref. 36), which is only present when the electron beam is placed in close proximity to the tip so that the outer tail of the electron focal spot grazes the tip surface. The plasmon contribution is well-separated from the main spectral features and can be easily subtracted from the spectra. Specifically, we identify the sideband populations by adopting a global fit function containing pseudo-Voigt profiles $V_{\mathrm{p}}(E)$ for the zero-loss peak and all photon sidebands (using symmetric amplitudes in $\pm|N|$). The plasmon peak at a loss energy E_{pl} was described by an asymmetric Gaussian $G_{\mathrm{pl}}(E)$:

$$P(E) = G_{\mathrm{pl}}\left(E - E_{\mathrm{pl}}\right) + \sum_{N=-\infty}^{\infty} a_{|N|} V_{\mathrm{p}}(E + N\hbar\omega) \tag{1}$$

Extended Data Fig. 4 shows a typical electron spectrum together with the fitted function. Note that an energetic shift of the sideband comb relative to the zero-loss peak due to electron chirp is absent in the case of a long excitation pulse relative to the electron pulse duration and does not have to be included in the fit. An evaluation of the strength of the plasmon band as a function of beam–surface distance allows for a positioning accuracy of ±5 nm.

Materials. The nanostructure employed in this work was prepared from a thin gold wire (diameter 250 μm) which was subjected to thermal annealing in vacuum (800 °C, 12 h) to increase crystallinity and reduce surface roughness[37]. A sharp tip (100 nm apex radius) was formed by electrochemical etching in aqueous hydrochloric acid (37%)[38]. Afterwards, the conical part of the tip (length ~50 μm) was cut by focused ion beam milling, transferred to a silicon frame and attached by ion-beam deposited platinum.

Quantum description using ladder operators. The interaction of electrons traversing an optical near-field has been theoretically treated several times in the past, usually by either direct integration of the time-dependent Schrödinger equation[6] or using a Green's function formalism[5,39]. The relation of this stimulated process to the spontaneous mechanisms observed by electron energy-loss spectroscopy and cathodoluminescence is discussed in ref. 39. Furthermore, it was also shown that a non-relativistic approach is sufficient as long as the relativistically correct electron dispersion (velocity as a function of energy) is used in the final result[40]. Here, we present an alternative derivation of inelastic near-field scattering probabilities using ladder operators, which allows for a succinct description.

The raising and lowering operators. Electrons in a time-harmonic electromagnetic field can experience energy loss or gain in multiples of the photon energy $\hbar\omega$, where ω is the frequency of the field. This allows us to treat the problem as a multilevel quantum system. Within the Schrödinger picture, the free-electron Hamiltonian H_0 does not depend on time, while the wavefunction $|\psi(t)\rangle$ of the electron is time-dependent. Thus, the total Hamiltonian for the interaction with the electromagnetic field in the velocity gauge is

$$H = H_0 + \frac{e}{m} pA \tag{2}$$

where A is the space- and time-dependent vector potential, and p, e and m are the electron momentum, charge and mass, respectively. For a time-harmonic vector potential, a natural basis set is composed of plane wave states $|N\rangle$ offset from the initial energy E_0 by an integer multiple N of the photon energy, where each state $|N\rangle$ is an eigenstate of the unperturbed Hamiltonian H_0: $H_0|N\rangle = (E_0 + N\hbar\omega)|N\rangle$. Thus, $|0\rangle$ is the initial state, and $|N\rangle$ corresponds to the state with $|N|$ absorbed/emitted quanta. The time-harmonic interaction Hamiltonian causes transitions between these basis states. In particular, the matrix elements between adjacent states of the form $\langle N+1|\frac{e}{m}pA|N\rangle$ will lead to considerable transition probabilities. In contrast, the coupling between states separated by more than one photon energy causes transition amplitudes rapidly oscillating in time (at multiple frequencies of ω), which prevents direct multiphoton transitions. (Note that multiphoton transitions will become possible by multiple actions of the field.)

In order to compute the coupling between neighbouring states, let us consider for simplicity a one-dimensional model with the time-harmonic vector potential $A = F(z)\sin(\omega t)/\omega$, where $F(z)$ is the spatial distribution of the electric field amplitude. To obtain the matrix elements $\langle N+1|\frac{e}{m}pA|N\rangle$, we use $|N\rangle$ in a plane wave form $L^{-\frac{1}{2}}\exp(ik_N z)$ in a finite spatial interval of length L, where $\hbar k_N$ is the electron momentum. In this representation, the matrix elements can be readily computed, for instance

$$\left\langle N+1\left|\frac{e}{m}pA\right|N\right\rangle=\frac{2\hbar v_N g}{L}\sin(\omega t),\quad g=\frac{e}{2\hbar\omega}\int\limits_{-L/2}^{L/2}F(z)\exp(-i\Delta kz)\mathrm{d}z \qquad (3)$$

where v_N is the electron velocity in the state $|N\rangle$, and $\Delta k\approx\omega/v_N$ is the electron momentum change (divided by $\hbar$). The dimensionless coupling constant g expressed in terms of a Fourier amplitude in equation (3) was introduced in a similar form as used in ref. 6. Physically, g describes the momentum component in the near-field distribution which allows for total energy and momentum conservation in the transition, that is, it represents the momentum change of an electron undergoing an energy transition of $\hbar\omega$. Regarding the integration limits in equation (3), at present, it is only important that the interval length L is larger than the extension of the near-field, as L will cancel out in the final result. It should be noted that for an initial energy much higher than the maximum number of absorbed or emitted photons, $E_0\gg|N|\hbar\omega$, the coupling matrix elements in equation (3) become practically independent of N, as does the velocity $v\approx v_N$. The presence of a single and universal coupling constant renders the present quantum system a nearly perfect example of an equal Rabi multilevel system[10]. The transitions in this system can be concisely described by introducing the raising and lowering operators $a^\dagger$ and a, respectively, as

$$|N+1\rangle=a^\dagger|N\rangle,\quad |N-1\rangle=a|N\rangle \qquad (4)$$

Note that, in contrast to the commonly employed ladder operators of a harmonic oscillator (which has a coupling constant scaling with $\sqrt{N}$), it follows from equation (4) that a and $a^\dagger$ commute: $aa^\dagger=a^\dagger a$. The essential parts of the interaction Hamiltonian then take a bi-diagonal form, which can be represented in the raising and lowering operators

$$\frac{e}{m}pA=\frac{2\hbar v}{L}\left(g^*a+ga^\dagger\right)\sin(\omega t)+\mathcal{O}(a^n,a^{\dagger n};n\geq 2) \qquad (5)$$

The higher order contributions can be neglected in the following, as they lead to negligible transition probabilities (see below), and terms on the main diagonal are absent because the spatial integral over the near-field distribution $F(z)$ (the case of $\Delta k=0$) vanishes.

The S-matrix. To obtain transition probabilities for electrons after passage through the near-field, it is convenient to switch to the interaction picture. Here, the lowering and raising operators become time-dependent: $a(t)$, $a^\dagger(t)$. In our case, they can be easily expressed in terms of a and $a^\dagger$ by the transformation

$$a(t)=\exp(-i\omega t)a,\quad a^\dagger(t)=\exp(i\omega t)a^\dagger \qquad (6)$$

and the interaction Hamiltonian turns into

$$H_{\mathrm{int}}(t)=\frac{2\hbar v}{L}\sin(\omega t)\left[\exp(-i\omega t)g^*a+\exp(i\omega t)ga^\dagger\right] \qquad (7)$$

where a and $a^\dagger$ denote the time-independent lowering and raising operators (see equation (4)). The temporal evolution of the quantum system can be treated in terms of a scattering matrix S, defined as a unitary transformation connecting asymptotic particle states $|\psi(\infty)\rangle=S|\psi(-\infty)\rangle$ before and after the interaction (for the time-dependence of the electron wavefunction during near-field transit, see ref. 5). This unitary operator S is given by the time-ordered exponent

$$S=T\exp\left(-\frac{1}{\hbar}\int\limits_{-\infty}^{\infty}H_{\mathrm{int}}(t)\mathrm{d}t\right) \qquad (8)$$

In the present case, the time-ordering T can be omitted because $a(t)$ and $a^\dagger(t)$ commute. With the choice of a finite support L of the basis states, the range of integration should in principle be limited to $\int_{-L/2v}^{L/2v}$, which will cancel out the ratio v/L appearing in equation (7) for the time-independent contributions. The terms oscillating at higher frequencies ($\int\exp(2i\omega t)\mathrm{d}t$ in equation (7) and higher order contributions from equation (5)) vanish in the limit of large L. This case of large L ($L>v/\omega$) corresponds to the experimental situation, in which the momentum states are well-resolved with respect to their energy difference $\hbar\omega$, and therefore, the passage to infinity can be carried out without loss of generality:

$$\frac{1}{\hbar}\int\limits_{-\infty}^{\infty}H_{\mathrm{int}}(t)\mathrm{d}t=\frac{g^*a-ga^\dagger}{i} \qquad (9)$$

Thus, the S-matrix in the interaction picture can be finally written as

$$S=\mathrm{e}^{ga^\dagger-g^*a} \qquad (10)$$

and interestingly, the scattering matrix takes on the form of a displacement operator[33].

The transition probabilities. Using the S-matrix, we can compute the probabilities of the transitions $|0\rangle\rightarrow|N\rangle$, given by $P_N=|\langle N|S|0\rangle|^2$. For this purpose, we first split the matrix exponent in equation (10) into a product of two exponents, $\exp\left(ga^\dagger-g^*a\right)=\exp\left(ga^\dagger\right)\exp\left(-g^*a\right)$. This separation is of course possible because a and $a^\dagger$ commute. Expanding the exponential operators in a Taylor series, we find

$$\exp\left(ga^\dagger\right)|0\rangle=\sum_{m=0}^{\infty}\frac{g^m}{m!}\left(a^\dagger\right)^m|0\rangle=\sum_{m=0}^{\infty}\frac{g^m}{m!}|m\rangle \qquad (11)$$

and analogously

$$\langle N|\exp(-g^*a)=\sum_{n=0}^{\infty}\frac{(-g^*)^n}{n!}\langle n|a^n=\sum_{n=0}^{\infty}\frac{(-g^*)^n}{n!}\langle N+n| \qquad (12)$$

Using equation (10) and the orthogonality relation $\langle N+n|m\rangle=\delta_{N+n,m,}$ we obtain

$$\langle N|S|0\rangle=\sum_{n=0}^{\infty}\frac{(-g^*)^n g^{n+N}}{n!(n+N)!}=g^N\sum_{n=0}^{\infty}\frac{\left(-|g|^2\right)^n}{n!(n+N)!} \qquad (13)$$

Comparing this result with the following series expansion for the Bessel function of the first kind

$$J_N(z)=(z/2)^N\sum_{n=0}^{\infty}\frac{(-z^2/4)^n}{n!(n+N)!} \qquad (14)$$

we finally obtain

$$P_N=J_N(2|g|)^2 \qquad (15)$$

Therefore, the probability of energy gain or loss is given in the form of Bessel functions of different order[6].

Propagation after interaction and Wigner function. The propagation of the electron wavefunction after interaction with the optical near-field can be described in terms of a unitary evolution operator $\exp(-iH_0t/\hbar)$, where H_0 is again the free-electron Hamiltonian. Let $\psi_p(t)$ be the wavefunction in momentum representation and p the electron momentum in the laboratory frame. The unitary evolution is then given by

$$\psi_p(t)=\mathrm{e}^{-iE_pt/\hbar}\psi_p(0) \qquad (16)$$

where $E_p=c\sqrt{(mc)^2+p^2}$ is the relativistic energy and m is the electron rest mass. In practice, the electron momenta p after the interaction are all very close to the initial (relativistic) electron momentum γmv, where v and γ are the initial electron velocity and the Lorentz contraction factor, respectively. For that reason, it is convenient to use 'shifted' momenta defined as $p'=p-\gamma mv$.

During the free propagation, the momentum distribution $|\psi_p(t)|^2$ remains unchanged because the unitary action only changes phases of the probability amplitudes $\psi_p(0)$. In contrast to the momentum distribution, the spatial density distribution will vary in time during the propagation. In a 'shifted' laboratory frame, the spatial representation of the wavefunction is given by the Fourier transformation

$$\psi(z-vt,t)=\frac{1}{2\pi}\int\limits_{-\infty}^{\infty}\mathrm{e}^{ipz/\hbar}\psi_p(t)\mathrm{d}p \qquad (17)$$

where $\psi_p(t)$ is normalized to unity and $z-vt$ is the shifted spatial coordinate. Figure 3a in the main text presents a computation of the probability density versus the arrival time of the wavepacket in a given plane as a function of the propagation distance between the interaction region and this plane.

The Wigner function of the quantum state (Fig. 3b in the main text) is given by

$$W(z-vt,p,t)=\frac{1}{\pi}\int\limits_{-\infty}^{\infty}\psi_{p+q}(t)\psi^*_{p-q}(t)\mathrm{e}^{-2iqz/\hbar}\mathrm{d}q \qquad (18)$$

It gives a phase space representation of the quantum state[33] and illustrates the propagation-induced pulse compression.

Numerical calculations. In order to elucidate the importance of a spatially narrow probing beam and a temporally stretched near-field excitation for the observation of multilevel Rabi oscillations, we performed numerical calculations to quantitatively characterize the influence of an incoherent averaging over (temporally and spatially) varying transition probabilities $P_N(\boldsymbol{r}_\perp,t)$, where t is the electron arrival time and $\boldsymbol{r}_\perp$ its position vector in the sample plane (perpendicular to the beam direction). In a different context, that is, in the description of laser-electron cross-correlations, similar computations were carried out in refs 5 and 6.

In a simplified geometry, the nanotip is modelled as a straight cylinder of a radius corresponding to that of the tip at the probing position ($r = 1\,\mu\mathrm{m}$), for which the scattered electric field can be analytically calculated within Mie theory[41]. The field enhancement at the surface of the tip shaft is about 1.4. In the approximated geometry, we obtain a Fourier amplitude of the scattered field of $\frac{g}{F_{\mathrm{inc}}} \approx 80.3\,\mathrm{V}^{-1}\mathrm{nm}$ (normalized to the incident field F_{inc}), in the same order of magnitude as in the experiments, and exponentially depending on the distance to the surface with a radial decay length of approximately 90 nm.

In Extended Data Fig. 5a, we study the effect of spatial and temporal averaging on the visibility of the Rabi oscillations by averaging over a disk-shaped beam and a Gaussian temporal distribution of different widths. The upper and lower graphs show the influence of a finite probing area and a reduction of the duration of sample excitation, respectively. Both for larger electron beam widths as well as shorter laser pulses driving the optical near-field, the Rabi oscillations exhibit weaker modulation and become substantially damped. Therefore, for the experimental electron pulse width of about 800 fs and a field decay of 90 nm, a probe radius around 10 nm and a near-field duration of 3.4 ps as in the experiments (black lines) allow for the observation of strongly modulated Rabi oscillations. For these experimental parameters, the sideband populations closely follow the analytical Bessel function dependence with minor deviations at higher fields (compare Extended Data Fig. 5b).

As shown in the main text, the sinusoidal phase modulation of the electron wavefunction by the interaction with the optical near-field leads to the formation of an attosecond pulse train after a certain distance of free propagation behind the interaction region. In the experiments, the electron pulse consists of a partially coherent ensemble of electrons, and we investigate here the robustness of the attosecond pulse train generation to an incoherent averaging over different coupling constants g and wavefunction evolutions with fluctuating initial energies. We find that an initial kinetic energy spread below the photon energy is fully sufficient for the formation of a clear attosecond pulse structure. Specifically, Extended Data Fig. 6 presents evolution maps of the electron pulse structure as a function of propagation distance, incoherently averaging simulations of pure states with an initial kinetic energy width of 0.1 eV each. In Extended Data Fig. 6a, b, the electron density is incoherently averaged over a range of kinetic energies $\Delta E = 0.7$ eV and 2.1 eV, respectively. At a range of 0.7 eV, the resulting electron density peak is practically indistinguishable from the ideal case of a pure state with 0.1 eV width (solid black line in Extended Data Fig. 6e). With increasing spread of the incoherent average, the peak begins to smear out, although its duration in the temporal focus is not notably enlarged even for a kinetic energy spread of 2.1 eV, three times larger than in the experiment.

An incoherent average over different coupling constants g experienced by the electrons within the electron beam area (lower row) has a different effect: for a small probing radius of 10 nm and a decay length of the coupling constant as used above, the peak width is not affected, but the depth of the temporal focus is broadened (Extended Data Fig. 6c). Increasing the probing radius to 50 nm (Extended Data Fig. 6d), that is, to a size substantially larger than in the experiment, the amplitude of the side lobes grows to ultimately affect the attosecond temporal resolution. In conclusion, the stability to perturbations in the coupling constant and the initial kinetic energy spread demonstrates that attosecond train generation will be observable under the given experimental conditions.

34. Park, S. T., Kwon, O.-H. & Zewail, A. H. Chirped imaging pulses in four-dimensional electron microscopy: femtosecond pulsed hole burning. *New J. Phys.* **14,** 053046 (2012).
35. Plemmons, D., Park, S. T., Zewail, A. H. & Flannigan, D. J. Characterization of fast photoelectron packets in weak and strong laser fields in ultrafast electron microscopy. *Ultramicroscopy* **146,** 97–102 (2014).
36. Egerton, R. F. Electron energy-loss spectroscopy in the TEM. *Rep. Prog. Phys.* **72,** 016502 (2009).
37. Schmidt, S. *et al.* Adiabatic nanofocusing on ultrasmooth single-crystalline gold tapers creates a 10-nm-sized light source with few-cycle time resolution. *ACS Nano* **6,** 6040–6048 (2012).
38. Ibe, J. *et al.* On the electrochemical etching of tips for scanning tunneling microscopy. *J. Vac. Sci. Technol. A* **8,** 3570–3575 (1990).
39. Asenjo-Garcia, A. & García de Abajo, F. J. Plasmon electron energy-gain spectroscopy. *New J. Phys.* **15,** 103021 (2013).
40. Park, S. T. & Zewail, A. H. Relativistic effects in photon-induced near field electron microscopy. *J. Phys. Chem. A* **116,** 11128–11133 (2012).
41. Schäfer, J., Lee, S.-C. & Kienle, A. Calculation of the near fields for the scattering of electromagnetic waves by multiple infinite cylinders at perpendicular incidence. *J. Quant. Spectrosc. Radiat. Transf.* **113,** 2113–2123 (2012).
42. Piazza, L. *et al.* Simultaneous observation of the quantization and the interference pattern of a plasmonic near-field. *Nature Comm.* **6,** 6407 (2015).

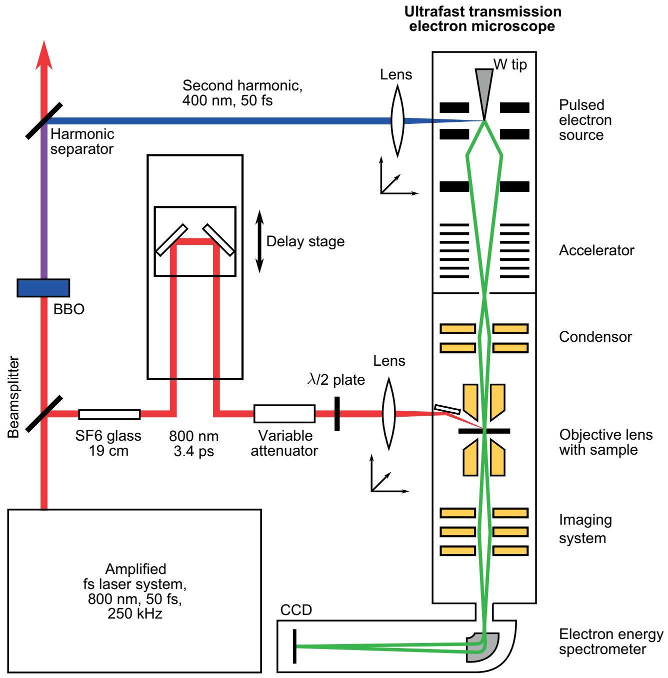

Extended Data Figure 1 | Experimental setup. Pulses from an amplified femtosecond (fs) laser system, at bottom left, are split into two optical beams. One of them is frequency-doubled in a β-barium borate (BBO) crystal and, after separation from the fundamental beam, focused (lens with numerical aperture 0.015, 50 cm focal length) onto the tungsten needle emitter (W tip) for the generation of electron probe pulses. The second beam (pump beam) is temporally stretched, attenuated and focused (lens with numerical aperture 0.014, 20 cm focal length) onto the sample within the TEM (angle of incidence, 55°). Relative timing between the electron probe and laser pump pulse is controlled by an optical delay stage. Optically-induced changes of the population of electron momentum states are recorded with an electron energy spectrometer. See Methods for details.

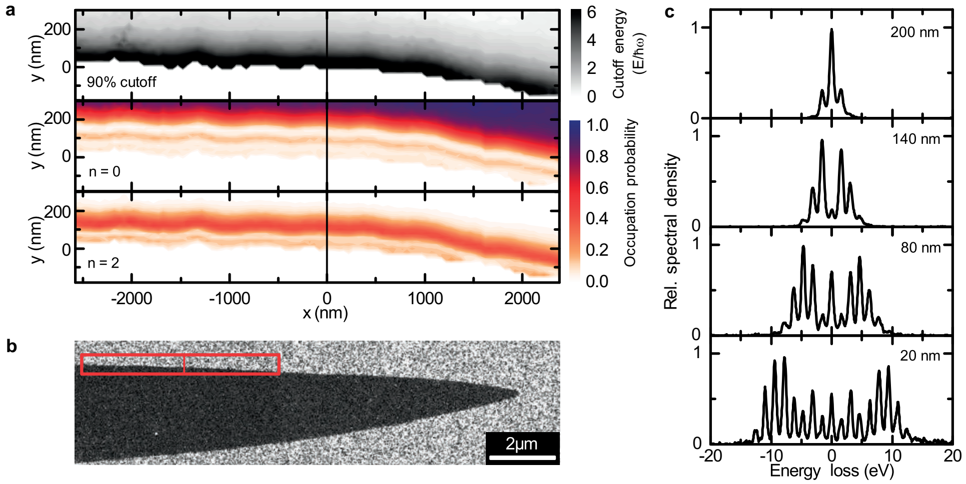

Extended Data Figure 2 | Spatial characterization of near-field scattering. **a**, Raster scan of the optically-induced electron energy gain and loss probability, characterized by the spectral cutoff (top panel) and the sideband populations of the zero loss peak (middle) and the second photon order (bottom). The field-dependent electron energy spectra shown in Fig. 2 of the main text were recorded at an *x* position indicated by the black line at the tip surface. A slow sample drift results in a scanning artefact in the *y* direction (jagged edge of the tip). For the results reported in the main text, a drift correction in the *y* direction was applied (see Methods section 'Data analysis and drift correction'). **b**, TEM image of gold tip. Red rectangle, scanning area displayed in **a**. **c**, Electron energy-loss spectra recorded along $x = 0$ with varying distance from the tip surface.

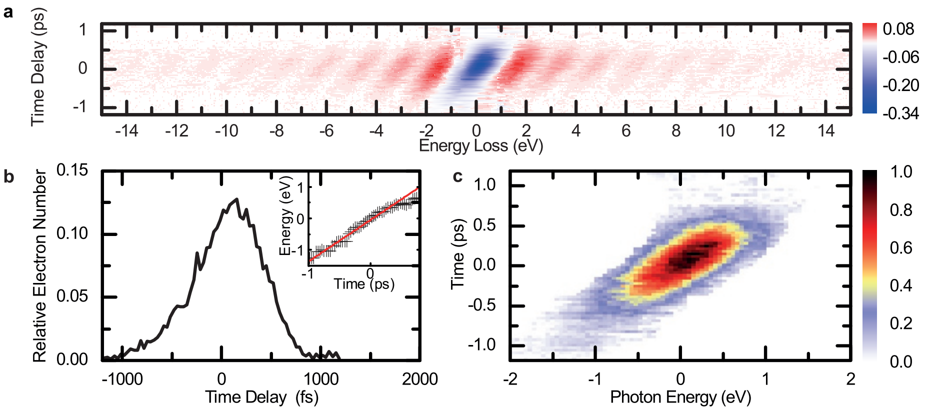

Extended Data Figure 3 | Pulse characterization by electron–photon cross-correlation. **a**, Differential electron energy-loss spectra as function of time delay (zero loss peak of width 1.3 eV subtracted; the colour scale shows the relative change of spectral density). **b**, Relative total scattering amplitude as function of time delay (inset, relative shift of photon sidebands with respect to zero loss peak). **c**, Energy- and time-resolved structure of the electron pulse (the colour scale shows the normalized electron density).

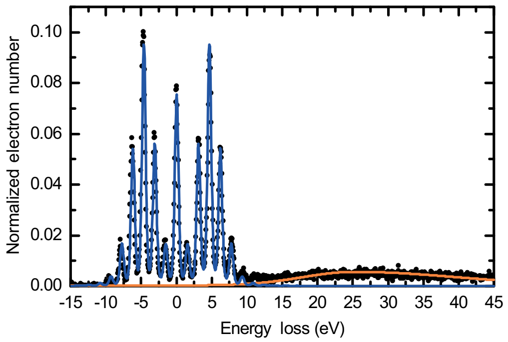

Extended Data Figure 4 | Evaluation of sideband populations. Example of electron energy spectrum (black dots) showing a number of photon sidebands and a weak low-loss plasmon contribution. Lines show fitted function used to extract sideband populations (blue) and the plasmon band (orange).

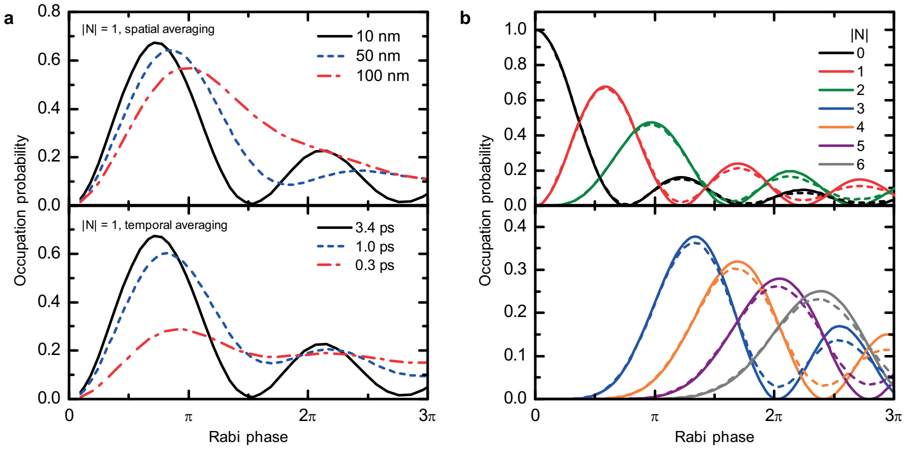

Extended Data Figure 5 | Influence of spatial and temporal averaging. **a**, Effect of electron beam size (top) and laser pulse duration (bottom) on the visibility of the Rabi oscillations in the order $|N| = 1$. For increasing electron beam size and decreasing laser pulse duration, the modulations are strongly damped. The black curves correspond to the experimental situation. **b**, Occupation probabilities of multiple spectral sidebands. Solid lines, Nth-order Bessel functions. Dashed lines, numerical calculations accounting for temporal and spatial averaging in the experiments.

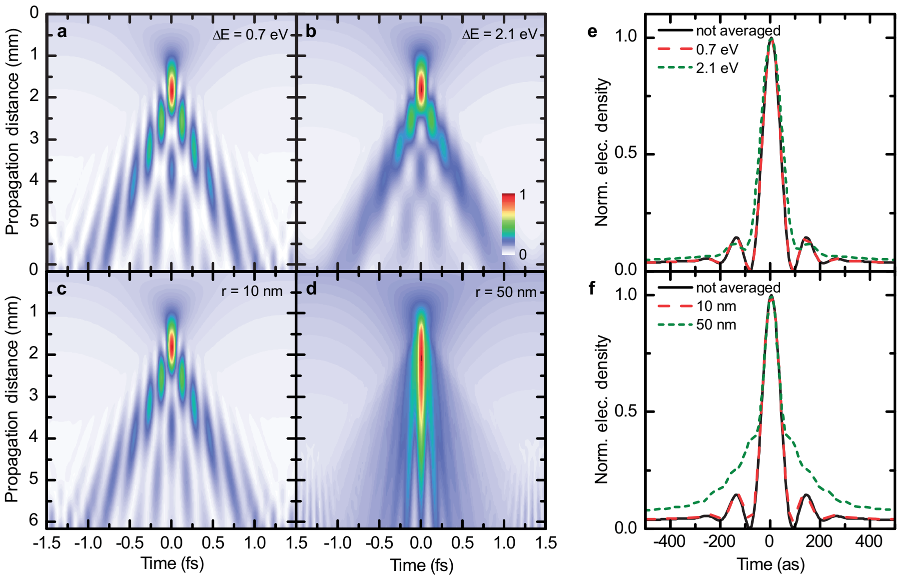

Extended Data Figure 6 | Robustness of attosecond pulse train generation. The influence of the electron beam's initial energy spread and lateral size on the temporal peak width of the generated pulse train are shown in the upper and lower rows, respectively. **a**–**d**, Evolution of the electron density as a function of propagation distance after the interaction with the optical near-field, incoherently averaged over the initial kinetic energy distribution (**a**, **b**) or the finite probing-area of the electron beam (**c**, **d**). A corresponding line profile at the propagation distance where the electron density peaks are at their maximum and form an attosecond pulse train is shown in **e** and **f**. For the experimental parameters used in this work (energy spread $\Delta E = 0.7$ eV FWHM and electron beam radius $r = 10$ nm), the peak width remains nearly unchanged as compared to the ideal (not averaged) case.